NeuroImage 188 (2019) 145–160

Contents lists available at ScienceDirect

NeuroImage

journal homepage: www.elsevier.com/locate/neuroimage

Analyzing the waveshape of brain oscillations with bicoherence

Sarah Bartz [a,d,*], Forooz Shahbazi Avarvand [b], Gregor Leicht [c], Guido Nolte [a]

[a] Department of Neurophysiology and Pathophysiology, University Medical Center Hamburg-Eppendorf, Martinistr. 52, 20246, Hamburg, Germany
[b] Siemens AG, Digital Factory Division, Motion Control, Machine Analytics Bad Neustadt an der Saale, Bayern, Germany
[c] Department of Psychiatry and Psychotherapy, University Medical Center Hamburg-Eppendorf, Martinistr. 52, 20246, Hamburg, Germany
[d] Berlin Institute of Technology, Machine Learning Laboratory, Berlin, Germany

ARTICLE INFO

Keywords:
Bicoherence
Waveshape
Alpha rhythm
Brain oscillation
Spatial filter
Schizophrenia

ABSTRACT

Oscillations are characteristic features of brain activity and have traditionally been categorized into frequency bands. Despite this categorization, brain oscillations have non-sinusoidal waveshape features, which have recently been discussed for their potential to mislead cross-frequency coupling measures. Waveshape characteristics deserve attention in their own right, as they are a direct reflection of the underlying neurophysiology and have shown to be altered in conditions such as Parkinson's disease. Here, we want to contribute to waveshape analysis in three steps: (1) While "shape" is most intuitively described in the time domain, complementary information is provided by frequency domain. In particular we show, that the bispectrum of an oscillation directly reflects waveshape properties such as differences in the steepness of its rise and decay phases, as well as differences in the duration of its crests and troughs. (2) Methods for the extraction of brain oscillations need to be chosen with care, as the ubiquitous use of bandpass filters causes waveshape distortions. We illustrate common problems and introduce a waveshape-preserving spatial filter for the purpose of waveshape analysis. (3) In an exemplary analysis of resting-state alpha rhythms, bicoherence provides evidence that shape characteristics of alpha rhythms exist on a spectrum. In addition, the bispectral view identifies significant mu rhythm anomalies in schizophrenia and suggests potential causes relating to waveshape.

1. Introduction

Waveshapes of brain oscillations are not sufficiently described by sinusoids. Instead, higher harmonics cause more complex waveforms, which have even been used to name particular rhythms such as the mu- or wicket rhythm. Recent publications have discussed the problem of so-called spurious cross-frequency coupling caused by non-sinusoidal waveshape features (Jones, 2016; Kramer et al., 2008). While such features have often been dismissed as an annoyance, their presence in a variety of brain oscillations is well documented (Cole and Voytek, 2017). Waveshape alterations of brain rhythms have been reported for certain diseases such as Parkinson's disease (Cole et al., 2016). Therefore, changes in oscillatory waveshape might give important insights into brain functioning and constitute a potential marker for disease. Despite the close link between waveshape and physiology, research often limits itself to a power comparison between experimental conditions. But not all aspects of neuronal oscillations are sufficiently reflected in a power spectrum. Waveshape features generally provide a much larger set of dimensions along which brain activity can be analyzed.

Here, we contribute to the waveshape analysis of brain oscillations in three ways:

- The quality of waveshape analysis can suffer, if oscillations are studied from sensor signals. Therefore, we propose a waveshape-preserving spatial filter to extract brain oscillations from channel mixtures. In contrast to other spatial filters (Cohen, 2017a, b), our filter does not rely on bandpass filtering of the input signal. It is thus able to extract brain oscillations, while leaving their harmonic structure—and consequently their waveshape—intact.
- Bicoherence has recently been shown to quantify phase-amplitude coupling (Avarvand et al., 2018; Kovach et al., 2017), while its relation to waveshape remains largely undiscussed. Studies of waveshape mostly rely on time-domain measures to characterize properties such as the sharpness and asymmetry of oscillatory peaks

* Corresponding author. Department of Neurophysiology and Pathophysiology, University Medical Center Hamburg-Eppendorf, Martinistr. 52, 20246, Hamburg, Germany.
E-mail address: s.bartz-schaechtelin@uke.de (S. Bartz).

https://doi.org/10.1016/j.neuroimage.2018.11.045
Received 22 May 2018; Received in revised form 15 November 2018; Accepted 25 November 2018
Available online 29 November 2018

(Cole et al., 2016). We show, that information about such shape characteristics can also be inferred from the bicoherence measure, with the advantage of receiving an additional resolution over frequencies.

- Reports on waveshape-altered brain oscillations in diseases imply, that some form of similarity exists in the brain rhythms of healthy subjects. To test evidence for such similarities, we conducted an exemplary bicoherence analysis of alpha oscillations in EEG resting-state recordings of healthy subjects and patients with schizophrenia. While bispectral information provides new perspectives on mu rhythm alterations in schizophrenia, we also find evidence for a spectral nature of alpha rhythm waveshapes in general.

1.1. Bicoherence and waveshape of alpha rhythms

The bicoherence of a signal is a function of two frequencies f_i and f_j. For a univariate signal $x(t)$ with Fourier transform $X_{(l)}(f)$ during epoch l, the bicoherence at the bifrequency $(f_i f_j)$ is computed as

$$\widehat{\mathrm{B}}(f_i,f_j) = \frac{1}{\mathrm{Norm}} \overbrace{\frac{1}{\mathrm{L}}\sum_{l=1}^{L} X_{(l)}(f_i)X_{(l)}(f_j)X^*_{(l)}(f_i+f_j)}^{\text{Bispectrum } B(f_i,f_j)}$$

$$= \frac{1}{\mathrm{Norm}} \frac{1}{\mathrm{L}}\sum_{l=1}^{L} \left(r_i\, r_j\, r_{i+j}\, e^{\phi_i+\phi_j-\phi_{i+j}}\right)_{(l)}.$$

As suggested by Shahbazi et al. (2014), we use a univariate normalization (Appendix A) and consider bicoherence as a complex quantity consisting of a magnitude and a phase part. Further, we refer to the phase of a specified bicoherence value as biphase.

In the second line of equation (1) we moved the epoch index l to the outer bracket and split each complex Fourier component into its magnitude r and phase part θ. This illustrates that each epoch is essentially represented by a complex number, which can be visualized as a vector in the complex plane. In each epoch, this vector's direction is determined by the phase relation of the Fourier components as $\phi_i + \phi_j - \phi_{i+j}$. The crucial insight is that the complex sum in (1) will take its maximum when this phase relation is the same during all epochs—this is analogous to the sum over a set of fixed-length vectors, which takes its maximum when all vectors point in the same direction. In its normalized

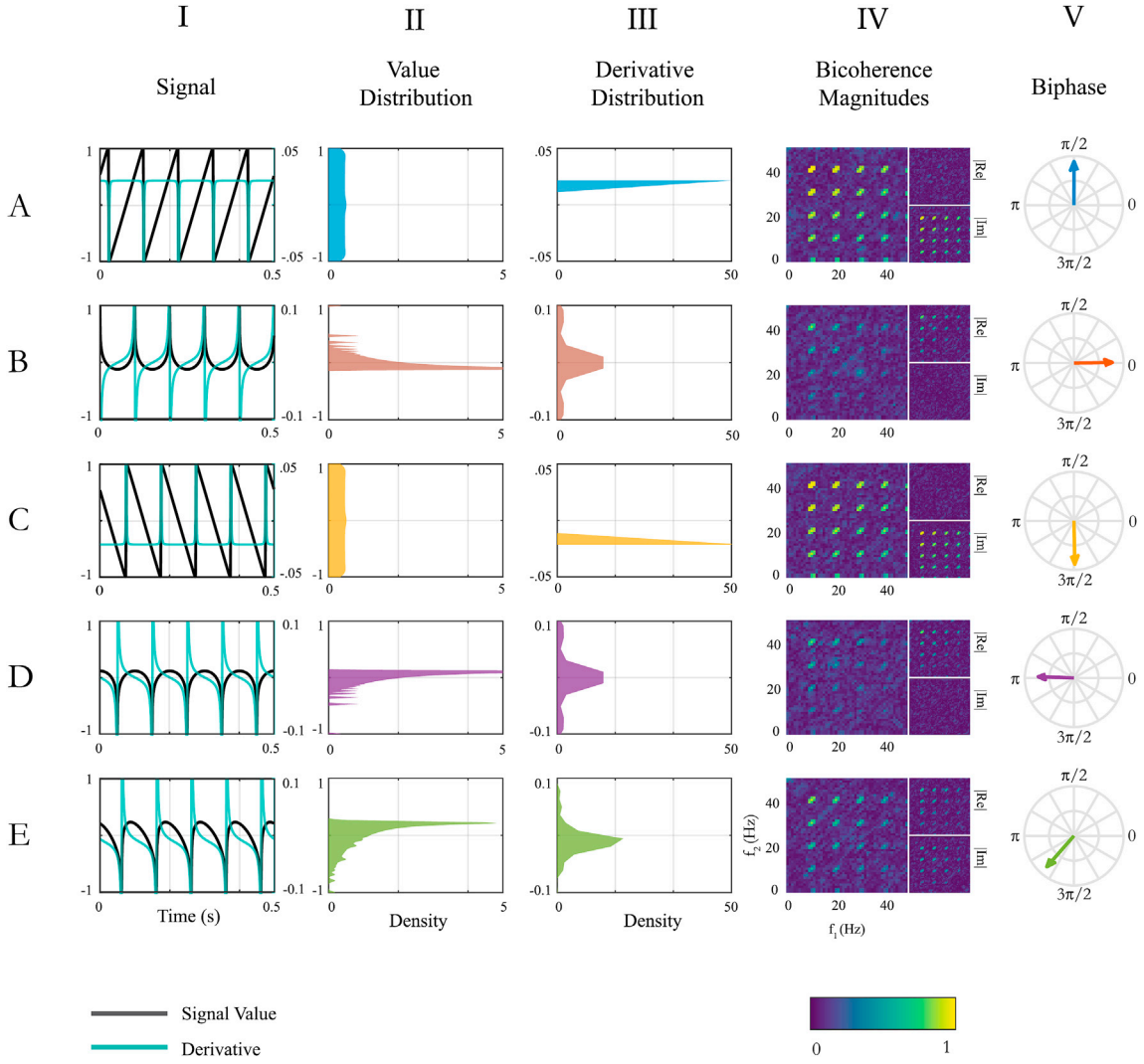

Fig. 1. . Five periodic signals with different symmetries and bispectral properties. All signals (A–E) have a fundamental frequency of 10 Hz and are composed of 200 harmonics (Appendix B). **(I)** Time courses and first derivatives. **(II)** Probability distribution of a signal's instantaneous values (its value distribution). **(III)** Probability distribution of a signal's scaled derivative values, the skewness of which quantifies time symmetry. **(IV)** Bicoherence magnitudes for pairs of frequencies from 0 to 50 Hz and corresponding magnitudes of the real and imaginary bicoherence pattern. **(V)** Phase of bicoherence (biphase) between pairs of harmonics. By construction, all signals (A–E) have the same biphase at all pairs of harmonics (Appendix B).

form, bicoherence magnitude therefore relates this sum to the sum resulting from perfectly aligned vectors of equivalent lengths.

While this form of bicoherence is the most intuitive one, it still bears the question of where the formula in (1) comes from: It can be derived by assuming stationarity of the zero-mean signal $x(t)$ and taking the double Fourier transform of its third-order cumulant function $C_3^x(\tau_1, \tau_2) = \langle x(t)x(t+\tau_1)x(t+\tau_2)\rangle$. This is analogous to a signal's power spectrum, which for zero-mean stationary signals is the Fourier transform of its second order cumulant — its autocorrelation function.

This origin of bicoherence as a cumulant spectrum helps us to show its relationship to waveshape features.

1.1.1. Signal skewness and peak-trough symmetry

If the distribution of a signal's instantaneous voltage values over time—we call it the value distribution— is symmetric, values above and below the mean value of the signal are equally likely to occur. A positively or negatively skewed value distribution results if a signal assumes lower values more often than higher ones or vice versa (Fig. 1B/D). We want to highlight, that a signal's skewness captures, what recent attempts to waveshape analysis have described as peak-trough symmetry (Cole and Voytek, 2018; Cole et al., 2016): For a mean-centered oscillation with peaks and throughs defined by its zero-crossings, the value distribution is skewed precisely if the signals period is not equally divided between troughs (low signal values) and peaks (high signal values). While skewness can be computed from the time domain signal, the bispectrum additionally shows how individual frequencies contribute to the total skewness of a signal: The unnormalized skewness of a real-valued and zero-mean stationary random process $x(t)$ is

$$\gamma^x = \langle x^3(t)\rangle = C_3^x(0,0),$$

where $C_3^x(0,0)$ is the third order cumulant function at time lags of zero. The unnormalized bicoherence—the bispectrum—is by definition related to this cumulant function by the Fourier transform

$$C_3^x(\tau_1,\tau_2) = \int\int_{-\infty}^{\infty} \mathrm{B}(f_1,f_2)\mathrm{e}^{i2\pi(f_1\tau_1+f_2\tau_2)}df_1df_2.$$

Therefore, for a discretely sampled process $x(t)$ it holds that

$$\gamma^x = C_3^x(0,0) = \sum_{f_1=-\infty}^{\infty}\sum_{f_2=-\infty}^{\infty} \mathrm{B}(f_1,f_2). \tag{2}$$

For a discrete and real-valued signal $x(t)$ with hermitian Fourier transform ($X(-f) = X^*(f)$), it follows that $B(-f_1,-f_2) = B^*(f_1,f_2)$. The unnormalized process skewness γ^x therefore becomes

$$\gamma^x = \sum_{f_1=-\infty}^{\infty}\sum_{f_2=-\infty}^{\infty} \Re(\mathrm{B}(f_1,f_2)).$$

Hence, the skewness of a signal is captured by the real part of its bispectrum.

1.1.2. Hilbert-/derivative skewness and rise-decay symmetry

For positive frequencies, the bispectrum of the Hilbert transform of $x(t)$ takes the form $B_{\mathscr{H}(x)}(f_1,f_2) = i\cdot B_x(f_1,f_2)$, for $f_1,f_2 > 0$. Only positive frequencies need to be considered due to the symmetry properties of the bispectrum for real-valued signals. From (2) we see that the skewness of the Hilbert transformed signal becomes

$$\gamma^{\mathscr{H}(x)} = -\sum_{f_1=-\infty}^{\infty}\sum_{f_2=-\infty}^{\infty} \Im(\mathrm{B}(f_1,f_2)).$$

Hence, the imaginary part of the bispectrum relates to the skewness of the Hilbert transform of $x(t)$, which in turn relates to its first derivative (slopes of the waveform) of the signal (Elgar, 1987). Derivative skewness describes what can intuitively be understood if we imagine walking along the signal's values in time: If the signal is the same whether we move forward or backward in time, its derivative distribution is symmetric and the imaginary part of its bispectrum is zero (Fig. 1I-II, B/D).

The derivative skewness of a signal captures a waveshape property, which has been referred to as rise-decay symmetry (Cole and Voytek, 2018; Cole et al., 2016): If the instantaneous value of an oscillation rises faster than it decays, this implies a respective asymmetry of the derivative distribution (neglecting the possibility of a baseline shift).

1.1.3. The biphase

The real- and imaginary part determine the phase of the complex bispectrum—the biphase defined as $\arctan2(\Im_{\widehat{B}}, \Re_{\widehat{B}})$ (Fig. 1V). The biphase therefore provides a summary of a signal's value- and derivative symmetries.

Some periodic signals like triangle- and square waves are symmetric in both—their value- and derivative distributions. The previous discussion implies, that in this case the bispectrum can neither have a real nor an imaginary part. In fact, the mentioned signals are only composed of odd harmonics and as the sum of odd harmonics is necessarily even, the bispectrum can only be zero.

1.1.4. Noise robustness of biphase estimates

A central property of waveshape analysis methods is their behaviour in the presence of noise and nonlinearities in the signals. We illustrate the noise robustness of biphase estimates by turning the idealized sawtooth oscillation (Fig. 1A) into a bursting oscillator (Fig. 2A) and adding various amounts of pink or brown noise (Fig. 2B and C): While the presence of noise still allows for unbiased estimates, it leads to an increased variance in the estimated biphases. The root-mean-square error (RMSE)—the root of the squared error which can be expected for individual biphase estimates—is therefore higher for lower signal-to-noise ratios (Fig. 2D). Even in cases where the target is not recognizable in the noisy signal (brown noise at an SNR of 0.01, pink noise at SNRs of 0.1 and 0.01) the RMSEs of individual biphase estimates are relatively low. While the precise RMSEs also depend on the amount of data used for estimation (2.5 s sampled at 1 kHz in our case), it still illustrates an advantage of using biphases: In cases where noise reduction through trials averaging is not possible—such as in resting-state EEG recordings—waveshape analysis in the time domain requires that the oscillation of interest is reasonably observable in the signal trace. If this is not the case, it has to resort to bandpass-filtering which always bears the risk of altering the waveshapes of interest.

1.1.5. Bicoherence patterns of alpha oscillations

Human EEG resting-state recordings show characteristic bicoherence patterns—thus patterns of bicoherence magnitude at several bifrequencies—at the sensor level. In a sample of 22 healthy subjects we make the following observations:

1. Almost all subjects show occipital bicoherence patterns with distinct peaks at bifrequencies involving an alpha-band frequency and its higher harmonics (Fig. 3A). The exact location of these bicoherence peaks varies consistently with the subject-specific alpha peak frequency f_p and is therefore likely to be caused by the occipital alpha rhythm.
2. In many but not all subjects, bicoherence patterns with multiple distinct peaks can be observed at central channels (Fig. 3B). As before, the peaks occur at bifrequencies involving a subject-specific alpha-band frequency and its higher harmonics, such that the mu rhythm is likely to be the underlying source signal. In contrast to the occipital patterns, the central patterns show a larger number of peaks, indicating a stronger presence of higher harmonics.

The bispectral view thus indicates, that the human resting-state EEG is dominated by two distinct alpha rhythms: the classical occipital alpha rhythm and the central mu rhythm.

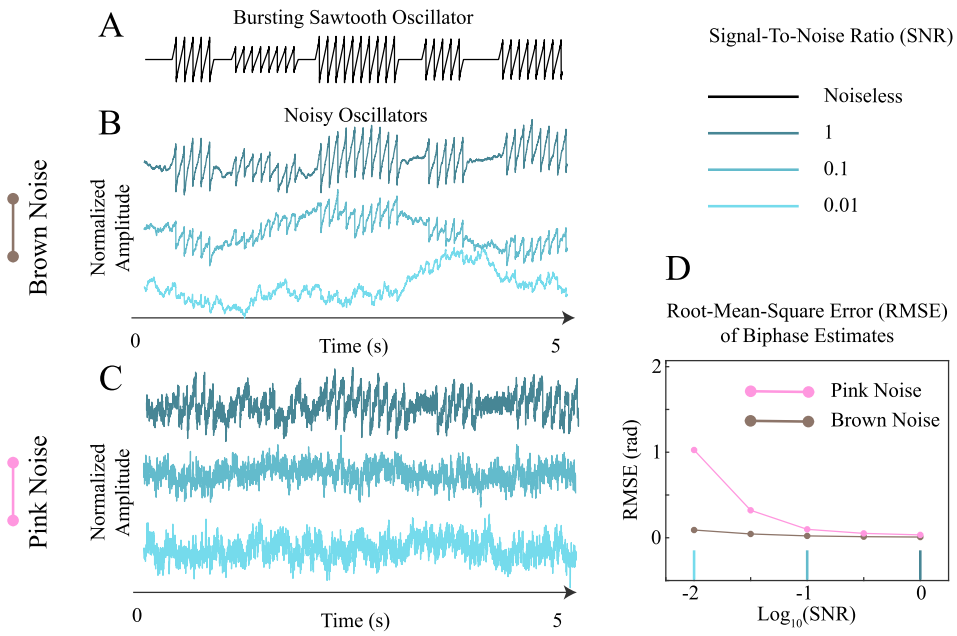

Fig. 2. Biphase estimation in the presence of noise.(A) A bursting oscillator with sawtooth waveshape features (biphase of $\pi/2$ between all harmonics) was used as target signal. In each trial, the oscillator was simulated for 2.5 s (at 1 kHz sampling frequency) with interburst intervals of uniformly distributed duration between 100 ms and 500 ms (always a full number of burst cycles). The duration of burst intervals were uniformly distributed between 500 ms and 1 s. Each bursting amplitude was chosen from a normal distribution with unit expectation and standard deviation of 0.2. **(B)** Snapshots of noisy oscillators created from (A) by adding brown noise at different signal-to-noise ratios (SNRs). **(C)** Snapshots of noisy oscillators created from (A) by adding pink noise at different SNRs. **(D)** Root-mean-square errors of biphase estimates for five SNRs between 0.01 and 1. Each RMSE was calculated from 50 repetitions.

We attempt an analysis of these two rhythms by using information which we have shown to be captured by the bispectrum. The described presence of bicoherence peaks between alpha harmonics highlights the importance of waveshape-preservation: Attempts to isolate brain rhythms from sensor signals (by ICA or other forms of spatial filters) should avoid bandpass filtering if waveshape features of oscillations are of relevance to the study. A large portion of this work is thus devoted to a spatial filter, which does not remove waveshape-defining harmonics and is therefore suited to extract oscillations for the purpose of waveshape analysis.

2. Methods

Matlab implementations of our methods can be found on GitHub https://github.com/scbartz/AnalyzingWaveshapeWithBicoherence

2.1. Spatial filter for waveshape analysis (harmonic power Maximisation—HPMax)

It is useful to isolate brain oscillations of interest from the sensor signals, before conducting bicoherence- or waveshape analysis. This can be understood by looking at how linear signal mixing changes bicoherence structure: A linear mixture of an alpha rhythm and a spectrally overlapping non-bicoherent signal will have a bicoherence pattern, which corresponds to the alpha rhythm pattern with weakened magnitudes, while the biphases are left unchanged. If the same alpha rhythm is linearly mixed with another spectrally overlapping signal, which has its own bicoherence peaks with biphases differing from the alpha biphases, the bicoherence pattern of the mixture will have bicoherence peaks with reduced magnitudes and altered biphases. It is even possible (although unlikely) that linear mixing of signals cancels preexisting bicoherence structure, if the constituent signals have opposing biphases.

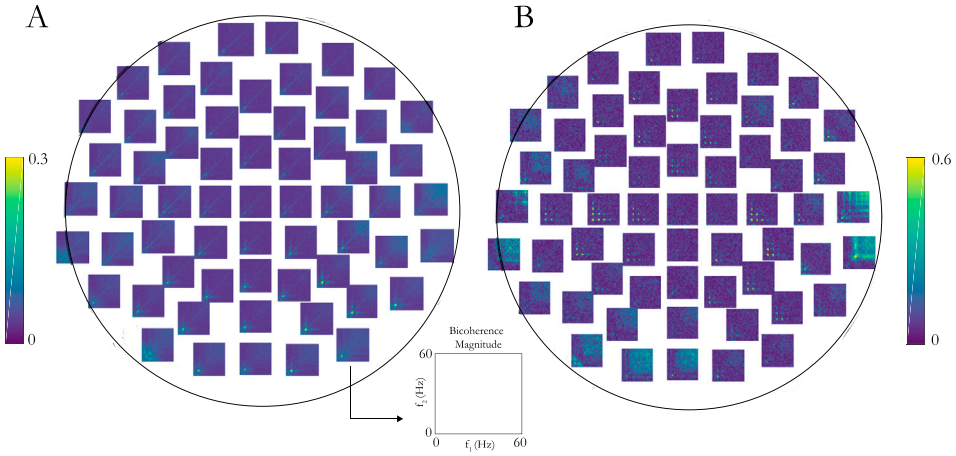

Fig. 3. Bicoherence patterns of signals at the channel level. Bicoherence values are shown for all bifrequencies between 1 and 60 Hz. **(A)** Average sensor level bicoherence patterns based on resting-state recordings of 22 healthy subjects. **(B)** Bicoherence patterns of a single subject with prominent occurrences of central bicoherence peaks.

2.1.1. HPMax derivation

Given the sensor signals from a multi-channel EEG recording $\mathbf{x}(t) \in \mathbb{R}^d$, we want to find a spatial filter $\mathbf{w} \in \mathbb{R}^d$, such that the resulting component $y(t) = \mathbf{w}^T\mathbf{x}(t)$ is likely to represent an alpha oscillation, if such an oscillation is present in the signal mixtures $\mathbf{x}$. Under the simplifying assumption of periodicity, alpha rhythms have nonzero power only at an alpha-band frequency and its higher harmonics. We turn this power-spectral property into a criterion, which can be imposed on the power spectrum P_y of a hypothetically extracted component $y(t)$. A criterion, which quantifies the described power-spectral peaks, is given by a global signal-to-noise ratio. Assuming that the future component y is composed of a signal- and a noise portion as

$$y(t) = y_s(t) + y_n(t),$$

we define the global SNR of y as

$$\mathrm{SNR}(y) = \frac{\sum_{h\in\mathscr{H}} P_{y_s}(f_{p\cdot h})}{\sum_{h\in\mathscr{H}} P_{y_n}(f_{p\cdot h})}, \tag{3}$$

where $\mathscr{H}$ contains the indicators of the harmonics to be used and $f_{p\cdot h}$ denotes the h^{th} harmonic frequency $h\cdot f_p$ of f_p. The SNR in (3) relates the total power at frequencies of the alpha oscillation to the total power of the noise at these frequencies. We denote the optimization of spatial filters according to this criterion as HPMax (Harmonic Power Maximisation). The quantities involved in (3) are unknown and need to be estimated. The noise power $P_{y_n}(f)$ of a component y at a single frequency f can be estimated as

$$\widehat{P}_{y_n}(f) = \frac{1}{2\Delta_f}\sum_{i=1}^{\Delta_f}\left(P_y(f-\Delta_{\mathrm{stop}}-i) + P_y(f+\Delta_{\mathrm{stop}}+i)\right).$$

The first parameter Δ_{stop} (in Hz) defines a frequency zone around the target frequency f, which is left out of the noise estimate. Such a parameter accounts for the fact, that power spectral peaks of neurophysiological recordings rarely show an abrupt decay from one frequency to the next. The second parameter Δ_f (in Hz) dictates the frequency interval used for the noise estimate, once the security zone defined by $f \pm \Delta_{\mathrm{stop}}$ has been left. A larger Δ_f can reduce the variance of the noise estimate, while at the same time it should be chosen small enough to avoid interference with higher harmonics of the target frequency f. The strategy of the above noise estimate is to approximate $P_{y_n}(f)$ by the average power at neighbouring frequencies, instead of estimating it at the target frequency f, directly. The underlying assumption is that the target oscillation does not have power at these surrounding frequencies, while the noise spectrum is not expected to change abruptly when moving from f to $f \pm (\Delta_{\mathrm{stop}} + \Delta_f)$. This method for noise estimation has already been used in other spatial filtering approaches like spatio-spectral decomposition (SSD) (Nikulin et al., 2011). Finally, based on these noise estimates, the SNR in (3) can be approximated as

$$\frac{\sum_{h\in\mathscr{H}} P_y(f_{p\cdot h})}{\sum_{h\in\mathscr{H}} \widehat{P}_{y_n}(f_{p\cdot h})} = \frac{\sum_{h\in\mathscr{H}} P_{y_s}(f_{p\cdot h}) + P_{y_n}(f_{p\cdot h})}{\sum_{h\in\mathscr{H}} \widehat{P}_{y_n}(f_{p\cdot h})}$$

$$\approx \mathrm{SNR}(y) + 1.$$

For a known signal component $y(t)$, we can therefore simply calculate the above SNR estimate. The goal however is to find a spatial filter $\mathbf{w}$, such that $y(t) = \mathbf{w}^T\mathbf{x}(t)$ maximizes this quantity. The crucial insight is, that every power valu e of a component y can be expressed as a function of the original signal $\mathbf{x}$ as

$$P_y(f) = \langle Y(f)Y^*(f)\rangle$$

$$= \mathbf{w}^T\langle \mathbf{X}(f)\mathbf{X}^*(f)\rangle\mathbf{w}$$

$$= \mathbf{w}^T\mathbf{C}_x(f)\mathbf{w},$$

where $\mathbf{C}_x(f)$ denotes the cross spectrum of the original signal $\mathbf{x}$ at frequency f. Indeed, we chose the form of the SNR in (3), such that it can be expressed as a function of the original multivariate signal $\mathbf{x}(t)$:

$$\frac{\sum_{h\in\mathscr{H}} P_y(f_{p\cdot h})}{\sum_{h\in\mathscr{H}} \widehat{P}_{y_n}(f_{p\cdot h})} = \frac{\mathbf{w}^T\overbrace{\left(\sum_{h\in\mathscr{H}}\Re\left(\mathbf{C}_{\mathbf{x}}(f_{p\cdot h})\right)\right)}^{:=\mathbf{S}}\mathbf{w}}{\mathbf{w}^T\underbrace{\left(\sum_{h\in\mathscr{H}}\Re\left(\widehat{\mathbf{C}}_{\mathbf{x_n}}(f_{p\cdot h})\right)\right)}_{:=\mathbf{N}}\mathbf{w}}. \tag{4}$$

The optimal spatial filter $\mathbf{w}^*$ can be found as

$$\mathbf{w}^* = \arg\max_{\mathbf{w}} \frac{\mathbf{w}^T\mathbf{S}\mathbf{w}}{\mathbf{w}^T\mathbf{N}\mathbf{w}}.$$

This optimization problem is of a well-known form called Rayleigh quotient. Using Lagrange multipliers, optimization problems involving Rayleigh quotients can be further reduced to solving a generalized eigenvalue problem of the form

$$\mathbf{S}\mathbf{w}_i = \lambda_i\mathbf{N}\mathbf{w}_i,$$

where $\mathbf{w}^*$ corresponds to the eigenvector associated with the largest eigenvalue. A proof of this relation, together with details on how to solve generalized eigenvalue equations, can be found in Appendix C.1.

2.1.2. Simulation setup

For performance testing we linearly mixed a non-sinusoidal target oscillation with different noise signals and compared HPMax and other extraction methods regarding their ability to reconstruct the target signal:

In addition to HPMax (with settings $\Delta_f = 1$ Hz, $\Delta_{\mathrm{stop}} = 8$ Hz and $\mathscr{H} = \{1,2,3\}$), we tested the previously mentioned SSD filter (Nikulin et al., 2011). In its original form, SSD suppresses unwanted signal components by applying the optimized spatial filter to a bandpass-filtered version of the input signal. To indicate the use of a bandpass filter, we denote this variant of SSD as SSD^+. In addition, we used a second variant of SSD in which we applied the spatial filter to the broadband input signal (SSD^-). Using these two variants, we can illustrate the interplay of noise suppression and waveshape preservation. Finally, we used TDSep (Ziehe and Müller, 1998), a high-performing source reconstruction method relying on signal decorrelation over time, which established a performance reference for each task difficulty.

As target signal we used a bursting oscillator, which we created by repeatedly concatenating bursting intervals (fundamental frequency of 10 Hz, sampled at 1 kHz) with activity-free interburst intervals. The duration of the bursting intervals was uniformly distributed between 0.5 and 1 s, but always contained an even number of cycles. The bursting amplitude was chosen from a normal distribution centered at 1 with a standard deviation of 0.2 (due to normalization of signals, the standard deviation is the only important quantity here). With equal probability, each burst was either a sawtooth oscillation or a modified sawtooth oscillation in which the weight factor of the h^{th} harmonic was changed from $1/h$ to $1/h^{3/2}$, causing a faster decay of power over harmonics and a higher resemblance to human alpha oscillations (Appendix B). The duration of each interburst-interval was chosen from a uniform distribution between 100 ms and 500 ms.

We used three different noise types with different spectral characteristics: While brown noise has more power at low frequencies, the spectrum of white noise is constant and thereby frequency-independent. The power of blue noise increases for higher frequencies. Mathemati-

cally, all three noise types are instances of power-law noise, in which the power at frequency f is proportional to $1/f^{\alpha}$ ($\alpha_{\text{brown}} = 2$, $\alpha_{\text{white}} = 0$, $\alpha_{\text{blue}} = -1$).

In each trial, the target oscillator was mixed with 20 independent noise instances into a set of 20 mixtures (Fig. 4A). We chose the number of sources and mixtures to be in line with electrode numbers of common EEG systems, while requiring as little computation time as possible. By using more sources than mixtures (20 noise sources plus the target source), we created an underdetermined system typically encountered in realistic EEG settings. The signal mixtures for a single trial were created in several steps: 1. We specified the noise type and generated 20 independent noise sources (for a duration of 5 min at 1 kHz sampling frequency). 2. We created a mixing matrix $\mathbf{A} \in \mathbb{R}^{20\times 20}$ with standard normal entries for the noise sources, resulting in 20 mixtures of the previously generated noise signals. 3. At last, we determined the average power of each noise mixture and added the target signal with a weight that would achieve a particular SNR with the noise mixture. The final signal mixtures resembled an actual EEG setting in which brain sources project to multiple electrodes.

We controlled the difficulty of the demixing task by specifying the relative strength of the target signal in the mixtures (SNR values log-spaced between 10^{-6} and 10^{2}). The range of SNR values was chosen as to cover the course of performances until saturation for all four methods. For each SNR we performed 30 repetitions, after which the curve of average performances over task difficulties had become reasonably smooth. Performances were assessed using the correlation between the extracted signal and the target oscillation. To overcome the arbitrariness of amplitude in spatial filtering procedures, each extracted signal was standardized and additionally represented by a sign-flipped version of itself.

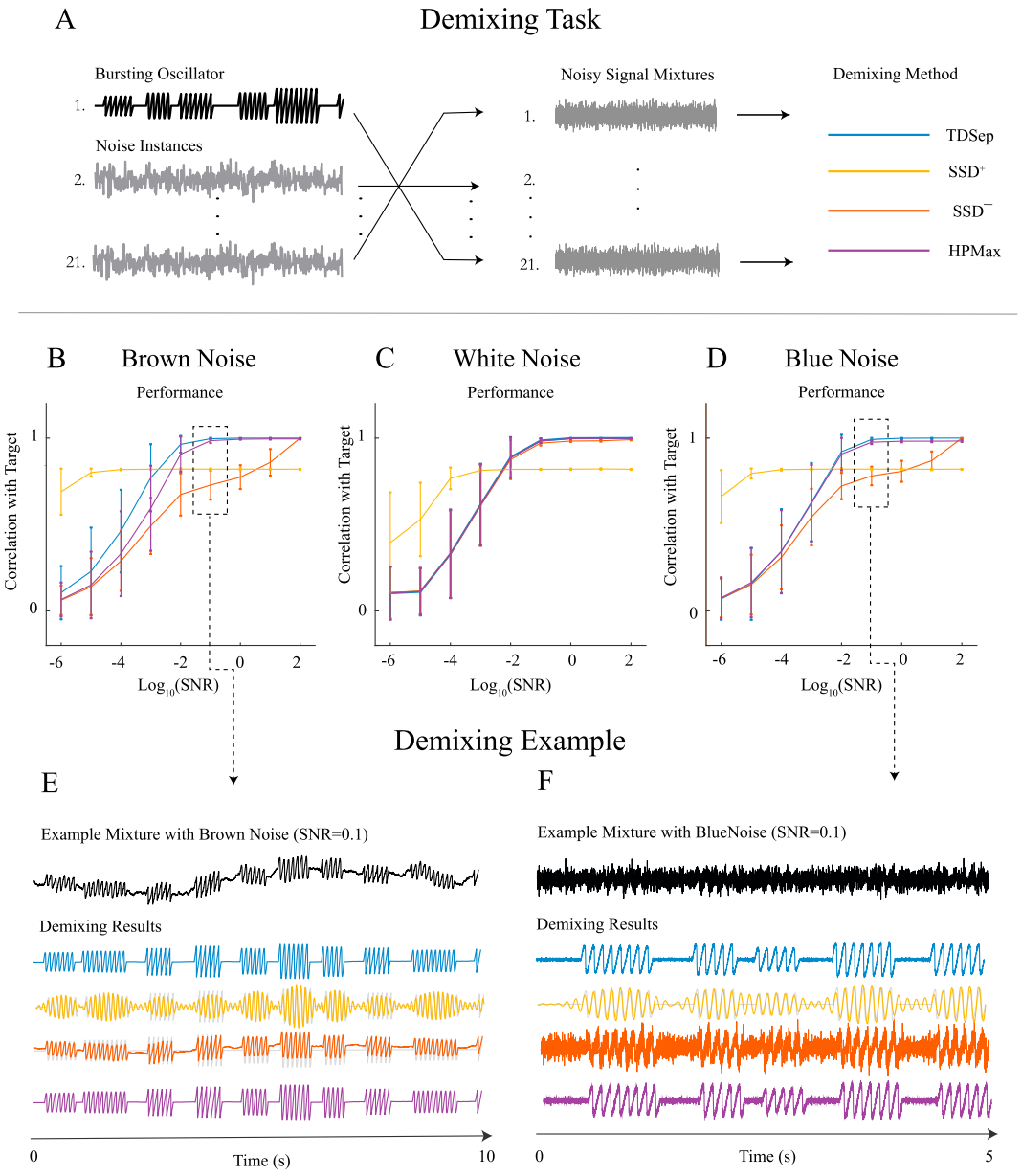

Fig. 4. Performance comparison of signal extraction methods.(A) Schematic overview of the signal extraction task: In each trial, a non-sinusoidal bursting oscillator was mixed with 20 instances of either brown-, white- or blue noise. The difficulty of the demixing task was varied by adjusting the signal-to-noise ratio (SNR) to 9 log-spaced values between 10^{-6} and 10^{2}. Extraction performance was measured using the correlation between extracted signals and the target oscillator. **(B-D)** Average extraction performances (over 30 trials) over SNRs for all methods and noise types. **(E–F)** Exemplary overview over demixing results for the different methods (at an SNR of 0.1 as indicated by the dashed arrows) for simulations using brown noise (E) and blue noise (F).

2.1.3. Comparison of methods

A performance comparison between SSD^+ and SSD^- illustrates their difficulties to simultaneously achieve noise suppression and waveshape preservation: At first sight, SSD^+ shows relatively strong performances even for low SNRs, while it quickly approaches a constant and suboptimal performance level as the task difficulty decreases for higher SNRs (Fig. 4B–D). This effective dealing with noise is mediated by the bandpass filtering involved in SSD^+ and it comes at the cost of waveshape destruction: The non-sinusoidal aspects of the target oscillator are removed in the sinusoidal signal extracted by SSD^+ (Fig. 4E–F, yellow signals). At high SNRs, the performance of SSD^+ is therefore limited by the correlation between the target signal and a noise-free sinusoid of the same fundamental frequency.

The difficulties encountered by SSD^- are opposite: While SSD^- preserves waveshape characteristics of the target, it is not designed to suppress noise in the broadband input signal. Instead, the SSD^- filter is optimized on bandpass-filtered versions of the input mixtures and therefore blind to noise in spectral regions removed by the bandpass filter. When such a spatial filter is subsequently applied to the broadband input, it often extracts large amounts of noise alongside the target signal (Fig. 4E–F, red signals). The severity of this effect depends on spectral properties of the noise type: If the noise has most power located around the fundamental frequency of the target oscillations, it is not removed during bandpass filtering and therefore seen by SSD^- during filter optimization. For this reason, SSD^- shows the worst performances in the case of blue and brown noise which—in contrast to white noise—have most of their power located away from the target frequency.

HPMax combines waveshape preservation with noise suppression and performs comparable to TDSep for white and blue noise (Fig. 4C–D). For brown noise, HPMax needs slightly higher SNRs than TDSep to reach optimal performances while still outperforming SSD^+ and SSD^- (Fig. 4B).

We do not intend to make general claims about particular noise types. Instead we want to show, that the performance of many spatial filters depends on the overlap between the frequency region of interest (for example the alpha band) and the frequency region the noise is most present. The fact, that blue noise leads to the most severe performance declines for SSD^+ is not explained by the presence of blue noise as such, but rather by the fact that the frequency region of interest lies in the alpha band at 10 Hz and the simultaneous weakness of blue noise in that region.

2.2. Extracting oscillations from resting-state EEG

We conducted a bicoherence analysis of alpha oscillations in resting-state EEG recordings of healthy subjects and patients with schizophrenia. The main goal was to show, how bicoherence can be used to analyze brain oscillations and how it provides information which is neglected by common power-spectral methods.

2.2.1. Subjects and recordings

We used continuous EEG resting-state recordings (sampled at 1 kHz with eyes closed for 10 min) of 22 patients with schizophrenia and 22 healthy controls. The data was provided by the Department of Psychiatry at the University Medical Center Hamburg-Eppendorf. A detailed description of the positioning of electrodes can be found in Appendix D.

2.2.2. Component extraction

For each subject we extracted alpha oscillations using HPMax ($\Delta_f = 3$ Hz, $\Delta_{\text{stop}} = 4$ Hz) and repeated this step for potential alpha peak frequencies between 8 Hz and 13 Hz. From each run of HPMax we retained the three best spatial filters (eigenvectors) instead of only one: This ensured, that different alpha rhythms with the same fundamental frequency could both be extracted, whereas the weaker rhythm would have otherwise been neglected. After artefact removal (Appendix F), we extended the representation of each extracted component by two more aspects: 1) For each component we performed an eLORETA source localization (see (Pascual-Marqui et al., 2006)) on its spatial topography and determined the location of maximum current density (LMCD) given in Neuromag coordinates. 2) We computed the component's bicoherence for several bifrequencies between 1 Hz and 60 Hz. Of particular importance for alpha rhythms are the bicoherence peaks $\widehat{B}(f_p, f_p)$, $\widehat{B}(f_p, f_{2p})$ and $\widehat{B}(f_p, f_{3p})$ and we refer to them by the simplified names H_{11}, H_{12} and H_{13}.

2.2.3. Measuring the strength of bicoherence peaks

The strength of a bicoherence peak is most intuitively described by the absolute value of bicoherence. Using bicoherence magnitude however, can be misleading: A broadband signal with constant spectral phases shows high bicoherence magnitudes at all bifrequencies. Aspects like recording noise can therefore increase the baseline magnitude of a signal's bicoherence. Especially while studying alpha rhythms it is useful to instead characterize strength by how much the bicoherence magnitude at a certain bifrequency stands out from the average magnitude at neighbouring bifrequencies as

$$\Phi\left(\widehat{B}(f_i, f_j)\right) = \left|\widehat{B}(f_i, f_j)\right| - \frac{1}{4} \sum_{\substack{(\Delta_i, \Delta_j) \\ \in \{-2,2\}^2}} \left|\widehat{B}\left(f_{i+\Delta_i}, f_{j+\Delta_j}\right)\right|.$$

2.2.4. Distinguishing occipital alpha- and mu rhythms

We devised a classification scheme to label each extracted component as either (a) occipital alpha rhythm (OA-component) or (b) mu rhythm (MR-component): The two alpha rhythms are expected to differ with respect to their LMCD_y-coordinate, which locates them on a line connecting the back to the front of the brain (axial-sagittal intersection line—AS-axis). As we further identified alpha rhythms to be the only source of bicoherence peaks during resting-state activity, clusters of components with strong bicoherence peaks should be observable in brain regions associated with the respective type of rhythm. Using kernel density estimation (Appendix E.1), we estimated the probability that components with strong bicoherence peaks occur at particular locations on the AS-axis. The resulting density estimate shows a bimodal distribution with an occipital and a central maximum (Fig. 5B). We used the minimum of this bimodal bicoherence density as the threshold to classify components as either OA- or MR-components.

2.2.5. Selecting representative components

For each subject, multiple components were extracted and sorted into one of two categories associated with a particular type of alpha rhythm. To allow for comparisons between groups of subjects, we lowered the number of components to a single best component per subject and component category. For this purpose, the extracted components of each subject were ranked with respect to their summed bicoherence strength

$$\Lambda = \Phi(H_{11}) + \Phi(H_{12}) + \Phi(H_{13}).$$

2.3. Statistical tests

We tested for differences in the average strength of bicoherence peaks H_{11}, H_{12} and H_{13} between

- patients and controls within the groups of OA-components and MR-components. In both component categories we used a two-sided permutation test ($\mathbf{H}_0 : \langle \Phi_{\text{Con}} \rangle = \langle \Phi_{\text{Pat}} \rangle$).
- OA-components and MR-components within the groups of patients and controls. In both groups of subjects we used a two-sided permutation test ($\mathbf{H}_0 : \langle \Phi_{\text{OA}} \rangle = \langle \Phi_{\text{MR}} \rangle$).

If the alpha rhythms represented by a group of components had great waveshape similarities, this should also be reflected by a similarity of

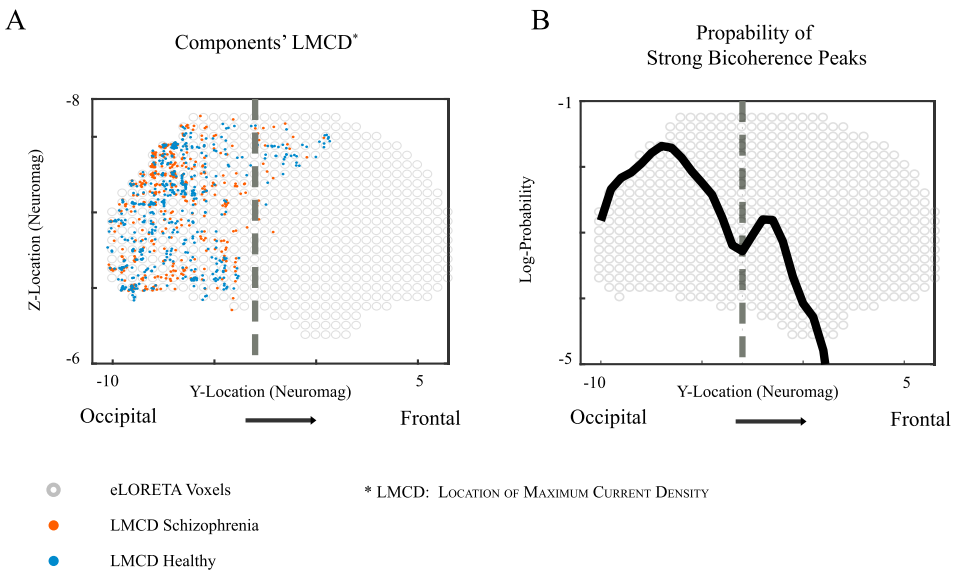

Fig. 5. (A) Sagittal distribution of the maximum eLORETA current density (LMCD) locations. Each point represents the location of highest estimated current density for a single signal component of patients (red) and controls (blue). For each subjects the plot shows LMCDs for all components, which passed our artefact rejection criteria—this implies a maximum of 18 depicted LMCDs per subject (best three HPMax components for 6 potential alpha peak frequencies). For illustrational purposes, the LMCD locations where randomly offset by small amounts (< 20% of distance between voxels (grey)) **(B)** Density estimate for the probability that LMCDs of components with strong bicoherence peaks fall onto particular y-location (occipital to frontal).

their biphases. To characterize biphase similarities we considered an equivalent random walk with unit steps taken in the direction of the biphases. The resulting normalized distance to the origin then served as a measure of similarity. This is, in a set of N components with biphases $\theta_1 \cdots \theta_N$ we computed

$$d(\theta_1 \cdots \theta_N) = \left| \frac{1}{N} \sum_{s=1}^{N} e^{i\theta_s} \right|. \quad (5)$$

The significance of non-uniformity was then determined with respect to the empirical probability distribution of $d(u_1 \cdots u_N)$ for $u_i \sim \mathcal{U}([0, 2\pi))$.

We tested the biphase uniformity at H_{11}, H_{12} and H_{13} for OA- and MR-components of patients and controls, separately. Further, we did not conduct this test if the average bicoherence strength in the set of components was < 0.1 (ID—insufficient data).

3. Results

For each hypothesis, we report the p-value category and the number of Bonferroni corrections n ($n = 0.05/p$-value) the effect can withstand (Fig. 6).

MR-components were identified for 11 of 22 patients and for 10 of 22 controls (Fig. 7). For the other subjects, none of the signal components extracted by HPMax passed the described 1/f-artefact rejection criteria. These numbers were consistent with our inspections of the raw EEG data. In both groups, OA-components were identified for all 22 subjects.

3.1. Bicoherence differences between subjects

MR-components showed significantly stronger peaks $H_{11}(p < 0.0005), H_{12}(p < 0.0001)$ and $H_{13}(p < 0.0005)$ in the group of controls

			Test Groups	H_{11}	H_{12}	H_{13}
Bipeak Strength	1.	MR	Patients/Controls ▲	*471	*714	*301
	2.	OA	Patients/Controls	N.S.	N.S.	N.S.
	3.	Patients	MR / OA ▲	*3	N.S.	*2
	4.	Controls	▲ MR / OA	*1	*5	*2
Biphase Uniformity	5.	MR (Patients)	-	*15	I.D.	I.D.
	6.	MR (Controls)	-	*25	$*>10^3$	$*>10^3$
	7.	OA (Patients)	-	$*>10^3$	$*>10^3$	I.D.
	8.	OA (Controls)	-	$*>10^3$	$*>10^3$	I.D.

OA = Occipital Alpha
MR = Mu Rhythm

Notation: □ $*n_1$
□ : uncorrected p-value category
n_1 : number of possible Bonferroni corrections
▲ : test group with larger mean of test statistic
N.S. : not significant
I.D. : insufficient data

Color Code
: p<0.05
: p<0.01
: p<0.005
: p<0.001
: p<0.0005
: p<0.0001

Fig. 6. Overview over p-values of statistical tests. For every hypothesis, the table shows the uncorrected p-value category and the number of multiple comparisons n_1—more precisely the number of possible Bonferroni corrections—-which can be corrected for while the respective result remains significant at a significance level of 0.05. In other words, $\alpha = 0.05/n_1$ represents the smallest significance level at which the effect would still be significant. **(1)** Differences between groups in the strength of bicoherence peaks of MR-components **(2)** As in (1), but for OA-components **(3)** Difference in average strength of bicoherence peaks between MR- and OA-components of patients **(4)** Difference in average strength of bicoherence peaks between MR- and OA-components of controls **(5–8)** Tests regarding the non-uniformity of the biphase distributions. **(5)** Tests for the MR-components of patients. **6)** Tests for the MR-components of controls. **7)** Tests for the OA-components of patients. **(8)** Tests for the OA-components of controls.

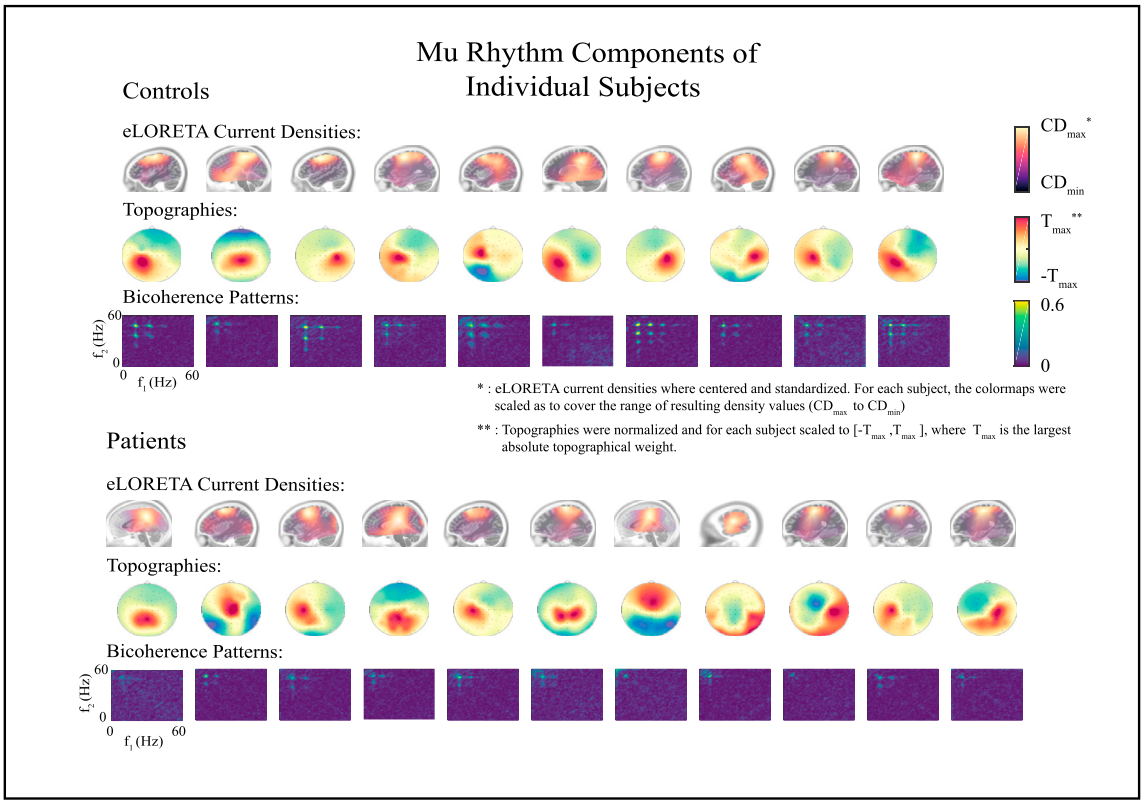

Fig. 7. Overview over selected MR-component of individual subjects. All MR-components (if identified) are shown by means of their associated eLORETA current density, their bicoherence pattern and spatial topography for patients and controls. If we identified more than one MR-component in a subject, we selected the one with the highest summed bicoherence strength (section 2.2.5).

compared to patients, while for OA-components no significant differences between patients and controls were identified.

3.2. Bicoherence differences between alpha rhythms

In controls, the average strength of bicoherence peaks was significantly higher in MR-components than in OA-components at all three bicoherence peaks H_{11} ($p < 0.05$), H_{12} ($p < 0.01$) and H_{13} ($p < 0.05$). In patients we observed the opposite effect for H_{11} and H_{13}: The average strength of these peaks was significantly higher in OA-components compared to MR-components ($p < 0.05$).

3.3. Biphase similarities

We tested the distribution of biphases at H_{11}, H_{12} and H_{13} with respect to their uniformity. The biphase distributions of MR-components showed significant non-uniformity at H_{11} in patients ($p < 0.01$), and for controls at H_{11} ($p < 0.005$), H_{12} ($p < 0.0001$) and H_{13} ($p < 0.0001$). OA-components showed significantly non-uniform biphase-distributions at H_{11} and H_{12} in patients and controls ($p < 0.0001$, in all four cases).

3.4. Power differences

For MR-components we conducted an additional analysis of power-spectral alpha peaks to be compared to results from the bispectral analysis: We identified alpha peaks in the component's power spectra using MATLAB's *findpeaks* routine and assessed their prominence (Appendix G) — a characterization of how much a peak stands out from its power-spectral surroundings.

In MR-components of controls we identified power-spectral peaks at the first and second alpha harmonic in all subjects and a peak at the third alpha harmonic in all but one control subject. In MR-components of patients we identified power-spectral peaks at the first harmonic in all subjects and at the second alpha harmonic for all but one subject. We did not find significant differences in the mean prominence of fundamental alpha peaks between the groups, while the power spectra of MR-components of controls showed significantly higher peak prominence at the second alpha harmonic ($p < 0.001$). Due to the absence of power-spectral peaks at the third alpha harmonic in most patients, we were not able to analyze group differences in peak prominence at this frequency.

We further identified multiple significant correlations between the strength of bicoherence peaks of MR-components and the prominence of alpha peaks in the associated power spectra. In patients we identified significant correlation between the bicoherence strength at H_{11} (depending on the first and second alpha harmonic) and the prominence of power-spectral peaks at the second alpha harmonic ($r = 0.71$, $p < 0.05$). In controls significant correlations were identified between strength at H_{11} and power-spectral peak prominence at the second alpha harmonic ($r = 0.69$, $p < 0.05$), between bicoherence strength at H_{12} and peak prominence at the second alpha harmonic ($r = 0.76$, $p < 0.05$) and the third alpha harmonic ($r = 0.77$, $p < 0.01$), as well as between bicoherence strength at H_{13} and power-spectral peak prominence at the fundamental alpha harmonic ($r = 0.69$, $p < 0.05$) and the third alpha harmonic ($r = 0.86$, $p < 0.01$).

4. Discussion

We illustrated that the bispectrum captures waveshape properties of brain oscillations. In particular the biphase of an oscillation reflects the presence of asymmetries in the relative duration of rise and decay phases and the relative duration of peaks and troughs. This relation implies, that waveshape characteristics of higher orders—such as skewness—continue to be captured in the frequency domain, and are not exclusively accessible in the time domain. The biphase of an oscillations therefore

provides an easy means to test for frequently reported waveshape alterations in particular diseases. While we discussed how the bispectrum (in particular the biphase) is affected by insufficient signal extraction and volume conduction effects, we introduced the HPMax spatial filter to analyze alpha oscillations in EEG resting-state recordings. One of our goals was to see, how similar alpha rhythm biphases are across subjects and whether they have a global tendency to one of the two described types of waveshape symmetries.

To be able to interpret results in terms of neurophysiology, we need to address two methodological aspects:

1. We discuss the evidence that components extracted by HPMax represent actual alpha rhythms. The HPMax optimization criterion is designed to target the power-spectral characteristics of alpha rhythms. If such a rhythm is present, it is very unlikely that any other signal component will be extracted instead. For cases in which no alpha rhythm was present, we used artefact rejection criteria which ensured that all included components displayed approximate $1/f$-spectral characteristics (Appendix F). The design of HPMax in combination with these criteria makes the erroneous inclusion of components, which do not represent alpha rhythms, unlikely. In the case of MR-components additional evidence is provided by the analysis of the component's power spectra, all of which exhibited a clear fundamental alpha peak.
2. We also address the procedure used to classify extracted signals as OA- and MR-components. Given the simplicity of our classification scheme, one could question the validity of the resulting label assignment to the extracted components. Yet, the classifiers decision boundary was not chosen arbitrarily but rather inferred from an observed gap in the bimodal distribution of bicoherence strength (Fig. 5B). In addition we argue, that almost every error or weakness of the classification procedure would weaken-, not strengthen, the statistical significance of identified differences between components.

4.1. Waveshape and symmetries of alpha rhythms

The biphases within a set—this is, the biphases belonging to the same component type, subject group and bicoherence peak—are not uniformly distributed across the phase space. With the exception of biphases belonging to vanishing bicoherence peaks, the biphases within a set are confined to subregions of $[0, 2\pi)$. While this structure in the biphase distribution can be determined visually (Fig. 8), it is additionally confirmed by our significance results. An interpretation in terms of waveshape suggests, that alpha rhythm characteristics in (healthy) subjects exist on a delimited spectrum and display varying degrees of signal- and derivative skewness. If this is the case, further research could study the consistency of biphases in subjects over time and as to what causes inter-individual waveshape differences. We further point out, that a particular biphase can result from different situations: While it can arise from a signal with constant bispectrum, it can also represent the average biphase of a signal with temporally varying bispectrum. While the

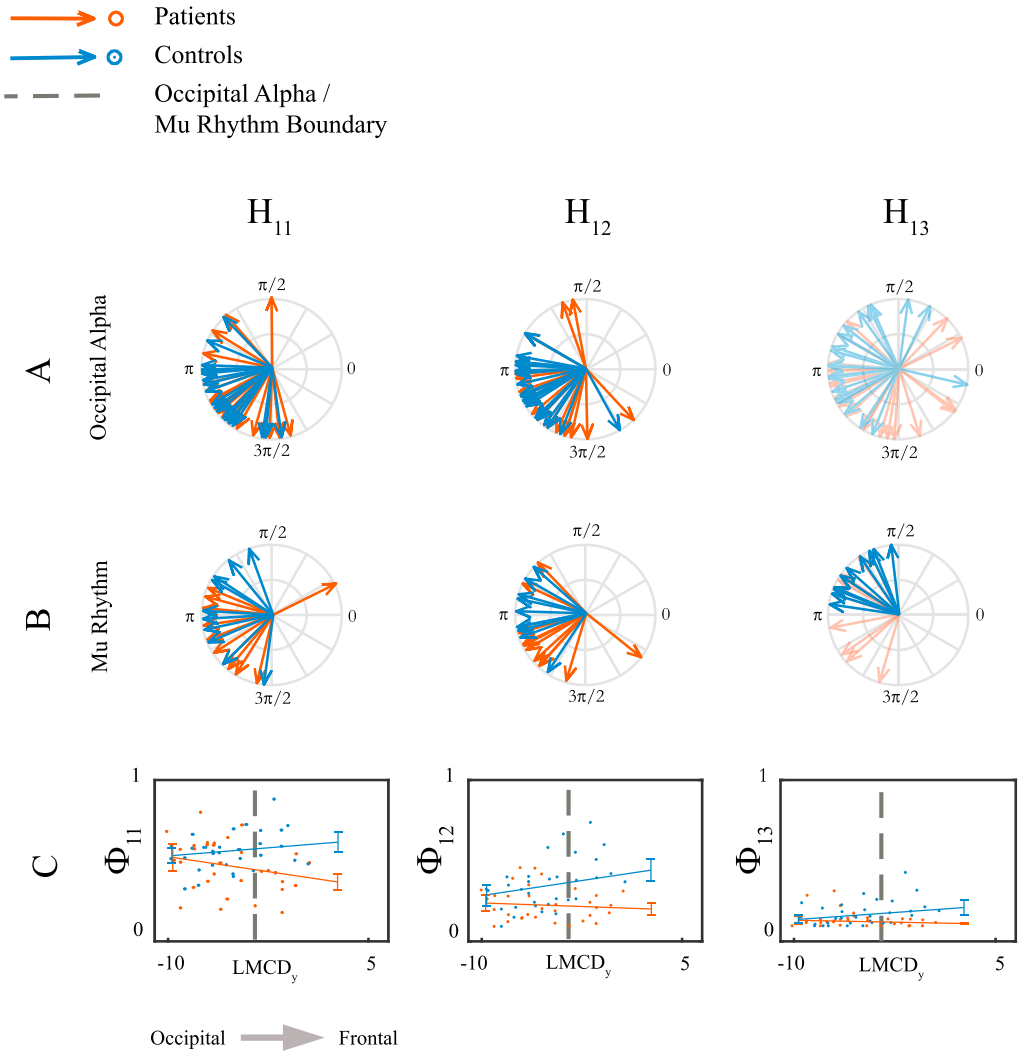

Fig. 8. Biphases and Strength of bicoherence peaks H_{11}, H_{12} and H_{13} for patients (red) and controls (blue). Groups of biphases (i.e. biphases belonging to the same component type and subject group) were grayed out, if their associated average bicoherence was weak ($\langle \Phi_{H_{1[1,2,3]}} \rangle < 0.1$). **(A)** Biphases of OA-components. **(B)** Biphases of MR-components. **(C)** Strength of bicoherence peaks plotted against LMCD_y-coordinates. The black dashed line marks the boundary between OA- and MR-components.

waveshape of the first signal exhibits constant amounts of skewness and derivative skewness, the waveshape of the second signal temporally fluctuates in these quantities. Such fluctuations of waveshape characteristics inevitably decrease the corresponding bicoherence magnitude, where the degree of bicoherence attenuations depends on the biphases of the fluctuation states: while the effect is weak if the bispectrum fluctuates between similar biphases, it can decrease the bicoherence magnitude to zero if the biphases oppose and cancel each other out.

4.2. Mu rhythm alterations in schizophrenia

We found bicoherence peaks of mu rhythms to be significantly weaker in patients with schizophrenia than in controls. Nonetheless, we observe a similar non-uniformity of associated biphases at peaks H_{11} and H_{12} (the vanishing bicoherence strength at H_{13} makes an interpretation of the biphases difficult). This resemblance to the biphase distribution of controls at first suggests, that the observed alterations of mu rhythms in schizophrenia are of a quantitative rather than qualitative nature. However, explanations exist at various levels:

- The simplest cause of reduced bicoherence strength is an overall decrease in power. Despite the efficiency of signal extraction methods, some amount of residual noise will be present in any extracted component. Consequently, a weaker mu rhythm will be more affected by such noise residues than a stronger rhythm, even if their waveshapes are qualitatively similar. In the case of intermittent brain rhythms such as the mu rhythm, an overall reduction in power could also result from fewer periods of intermittent activity. If the MR-components of patients just contained higher amounts of residual noise (with a common neurophysiological power spectrum resembling that of pink or brown noise), the greatest difference in the prominence of power-spectral peaks between patients and controls should be observed at the fundamental alpha frequency. While our analysis of alpha peak prominence revealed significant differences between the groups at the second alpha harmonic, no such differences were found at the fundamental alpha frequency. A lower signal-to-noise ratio in MR-components of patients therefore seems to be an insufficient explanation for the observed bispectral differences.
- Another possible explanation is given by differences in the spectral composition of mu rhythms in patients, such as a relative decrease of power at higher harmonics leading to mu rhythms with a more sinusoidal waveshape. Our analysis however identified reduced strength at all bicoherence peaks in patients, such that differences in spectral composition of mu rhythms are not a sufficient explanation by themselves.
- A third possible cause are the previously mentioned waveshape fluctuations over time. The underlying bispectral fluctuations can explain the observed decrease in bicoherence strength between harmonics.

These explanations vary in their consistency with existing knowledge about mu rhythms in schizophrenia: Mu rhythms have been linked to the mirror neuron system (MNS) in monkeys, in that they are both responsive to the execution, as well as the perception of action (Di Pellegrino et al., 1992; Keysers et al., 2003; Kohler et al., 2002). In particular it was suggested, that suppression of the mu rhythm could reflect the activity of mirror neurons (Muthukumaraswamy et al., 2004; Muthukumaraswamy and Johnson, 2004). Many symptoms of schizophrenia in turn have been linked to deficits in the mirror neuron system (McCormick et al., 2012; Iacoboni and Dapretto, 2006; Enticott et al., 2008). The presence and severity of negative symptoms of schizophrenia have been shown to negatively correlate with MNS activity (Sponheim et al., 2000) and consequently a lesser degree of mu suppression in response to action or action perception. These described differences concern the temporal prevalence of intermittend mu activity in patients, while not making claims about qualitative differences in waveshape. These described differences however, cannot sufficiently explain our observations: Reduced mu suppression in schizophrenia should make the rhythm more powerful and measurable in patients. As this would imply an increase in overall mu power, a power-based explanation of the observed bicoherence differences is rendered inconsistent.

At last, we discuss the possibility that our results are not caused by differences in mu rhythms at all: Systematic differences in EEG resting-state activity in schizophrenia—such as systematic differences in the amount of neural noise—could lead to a systematic increase of residual noise in signal components of patients. While we have shown that HPMax is mostly independent of the spectral characteristics of noise, we ultimately cannot rule out a bias of this kind.

4.3. Summary and outlook

In summary, our work contributes to a methodological foundation for the waveshape analysis of brain oscillations. We illustrated commonly occurring problems when unsuited spatial filters are used to extract brain oscillations for waveshape analysis and introduced HPMax as a suitable alternative. While attempts to waveshape analysis have been made in the time domain, we have shown that the time-frequency duality of the Fourier transform holds for waveshape characteristics as well: We have shown how the bispectrum provides a frequency decomposition over third-order waveshape statistics, like the skewness of a time series. In an exemplary analysis of resting-state EEG recordings our bicoherence analysis indicates that alpha waveshapes in resting-state exist on a spectrum, thereby encouraging further research at the level of single subjects. Based on bicoherence analysis we identified mu rhythm differences in subjects with schizophrenia, for which we also provided possible explanation at the waveshape-level. The explanation, which relates differences in bicoherence to a higher temporal variability in waveshape characteristics, could be further tested with the help of suitable time-domain methods. The close relation between waveshape characteristics of brain oscillations and their underlying neurophysiological processes highlights the potential of bicoherence in this regard. Future research could provide an even more detailed link between graphical characteristics of bicoherence patterns and underlying waveshape characteristics, thereby providing a more efficient and diverse approach to the analysis of brain oscillations.

Competing interests

The authors declare that no competing interests exist.

Acknowledgement

This research was partially funded by the German Research Foundation (DFG, SFB936 A3, C6, Z3 and TRR169, B1, B4), from the Landesforschungsfoerderung Hamburg (CROSS, FV25).

Appendix A. Bicoherence

If the bicoherence measure is appropriately normalized, its magnitude values range between zero and one. The literature on bicoherence varies with respect to the normalization that is used. Following the advice in Shahbazi et al. (2014), we used the univariate normalization

$$\mathrm{Norm}(f_1,f_2) = \Psi(f_1)\Psi(f_2)\Psi(f_1+f_2),$$

with

$$\Psi(f) = \left(\frac{1}{L}\sum_{l}^{L} \left|\mathbf{X}_{(l)}[f]\right|^3\right)^{1/3}.$$

Appendix B. Composition of Harmonic Signals

All harmonic signals were generated according to

$$x(t) = \sum_{h}^{N_H} \frac{1}{h}\cos(2\pi h f_0 t + (h-1)\cdot\phi_0),$$

with

$$\phi_0 = \begin{cases} \frac{3}{2}\pi, & \text{if } x \text{ is sawtooth (Fig. 1A)} \\ 2\pi, & \text{if } x \text{ is spiking (Fig. 1B)} \\ \frac{5}{2}\pi, & \text{if } x \text{ is inverse sawtooth (Fig. 1C)} \\ 3\pi, & \text{if } x \text{ is downward spiking (Fig. 1D)} \\ \frac{7}{4}\pi, & \text{if } x \text{ is hybrid (Fig. 1E),} \end{cases} \tag{B.1}$$

where the number of harmonics is indicated by N_H.

Appendix C. HPMax

Appendix C.1. Derivation

$$\frac{\sum_{h\in\mathscr{H}} P_y(f_{p\cdot h})}{\sum_{h\in\mathscr{H}} \widehat{P}_{y_n}(f_{p\cdot h})} = \frac{\sum_{h\in\mathscr{H}} \left\langle Y(f_{p\cdot h}) Y^*(f_{p\cdot h})\right\rangle}{\sum_{h\in\mathscr{H}} \left\langle \widehat{Y}_n(f_{p\cdot h})\widehat{Y}_n^*(f_{p\cdot h})\right\rangle}$$

$$= \frac{\sum_{h\in\mathscr{H}} \left\langle \mathbf{w}^T\mathbf{X}(f_{p\cdot h})\left(\mathbf{w}^T\mathbf{X}(f_{p\cdot h})\right)^*\right\rangle}{\sum_{h\in\mathscr{H}} \left\langle \mathbf{w}^T\widehat{\mathbf{X}}_n(f_{p\cdot h})\left(\mathbf{w}^T\widehat{\mathbf{X}}_n(f_{p\cdot h})\right)^*\right\rangle}$$

$$= \frac{\sum_{h\in\mathscr{H}} \mathbf{w}^T\left\langle \mathbf{X}(f_{p\cdot h})\mathbf{X}^*(f_{p\cdot h})\right\rangle\mathbf{w}}{\sum_{h\in\mathscr{H}} \mathbf{w}^T\left\langle \widehat{\mathbf{X}}_n(f_{p\cdot h})\widehat{\mathbf{X}}_n^*(f_{p\cdot h})\right\rangle\mathbf{w}}$$

$$= \frac{\sum_{h\in\mathscr{H}} \mathbf{w}^T\mathbf{C}_{\mathbf{x}}(f_{p\cdot h})\mathbf{w}}{\sum_{h\in\mathscr{H}} \mathbf{w}^T\widehat{\mathbf{C}}_{\mathbf{x_n}}(f_{p\cdot h})\mathbf{w}}$$

$$= \frac{\mathbf{w}^T\left(\sum_{h\in\mathscr{H}} \mathbf{C}_{\mathbf{x}}(f_{p\cdot h})\right)\mathbf{w}}{\mathbf{w}^T\left(\sum_{h\in\mathscr{H}} \widehat{\mathbf{C}}_{\mathbf{x_n}}(f_{p\cdot h})\right)\mathbf{w}}$$

$$= \frac{\mathbf{w}^T\mathbf{S}\mathbf{w}}{\mathbf{w}^T\mathbf{N}\mathbf{w}}, \tag{C.1}$$

where

$$\mathbf{S} := \sum_{h \in \mathcal{H}} \Re\left(\mathbf{C}_{\mathbf{x}}\left(f_{p \cdot h}\right)\right)$$

and

$$\mathbf{N} := \sum_{h \in \mathcal{H}} \Re\left(\widehat{\mathbf{C}}_{\mathbf{x_n}}\left(f_{p \cdot h}\right)\right).$$

We show why the imaginary part of the cross spectra vanishes: By decomposing a generic cross-spectral matrix $\mathbf{C}$ into a real- and imaginary part $\Re(\mathbf{C})$ and $\mathfrak{F}(\mathbf{C})$, it can be seen why the latter vanishes in the quadratic expression in (C.1). Since $\mathfrak{F}(\mathbf{C})$ is skew-symmetric, hence $\mathfrak{F}(\mathbf{C})^T = -\mathfrak{F}(\mathbf{C})$, it holds that

$$\mathbf{w}^T\mathbf{C}\mathbf{w} = \mathbf{w}^T\Re(\mathbf{C})\mathbf{w} + \underbrace{i\sum_{k,l}(\mathbf{w})_k \cdot (\mathbf{w})_l \cdot (\mathfrak{F}(\mathbf{C}))_{kl}}_{=0}.$$

Appendix C.2. Equivalence of Optimization Problems

The term in (C.1), which we intend to maximize, is of a well-known form called Rayleigh quotient. The optimal spatial filter $\mathbf{w}^*$ can be found as

$$\mathbf{w}^* = \arg\max_{\mathbf{w}} \frac{\mathbf{w}^T\mathbf{S}\mathbf{w}}{\mathbf{w}^T\mathbf{N}\mathbf{w}}. \tag{C.2}$$

Optimization problems involving Rayleigh quotients can be further reduced to solving a generalized eigenvalue problem of the form

$$\mathbf{S}\mathbf{w}_i = \lambda_i\mathbf{N}\mathbf{w}_i, \tag{C.3}$$

where $\mathbf{w}^*$ corresponds to the eigenvector associated with the largest eigenvalue. The transformation into an eigenvalue problem involves the following steps: Optimization of the Rayleigh quotient in (C.2) is equivalent to the constrained quadratic optimization problem

$$\max_{\mathbf{w}} \mathbf{w}^T\mathbf{S}\mathbf{w} \text{s.t.} \mathbf{w}^T\mathbf{N}\mathbf{w} = 1. \tag{C.4}$$

To show the equivalence of the optimization problems (C.4) and (C.2), we start with a solution $\mathbf{w}_2$ to (C.4), hence

$$\mathbf{w}_2 = \arg\max_{\mathbf{w}:\mathbf{w}^T\mathbf{N}\mathbf{w}=1} \mathbf{w}^T\mathbf{S}\mathbf{w},$$

$$\mathbf{w}_2^T\mathbf{S}\mathbf{w}_2 = O_2.$$

In addition we assume the existence of a unique solution $\mathbf{w}_1 \neq \mathbf{w}_2$ to (C.2):

$$\mathbf{w}_1 = \arg\max_{\mathbf{w}} : \frac{\mathbf{w}^T S\mathbf{w}}{\mathbf{w}^T N\mathbf{w}}.$$

Since $\mathbf{w}_1$ maximizes (C.2), it follows that

$$\frac{\mathbf{w}_1^T\mathbf{S}\mathbf{w}_1}{\mathbf{w}_1^T\mathbf{N}\mathbf{w}_1} > \frac{\mathbf{w}_2^T\mathbf{S}\mathbf{w}_2}{\mathbf{w}_2^T\mathbf{N}\mathbf{w}_2} \tag{C.5}$$

However since $\mathbf{S}$ and $\mathbf{N}$ are positive semi-definite matrices (e.g. $\mathbf{w}^T\mathbf{S}\mathbf{w} \geq 0, \forall \mathbf{w} \in \mathbb{R}^d$), we can rewrite the optimization problem (C.2) as

$$\frac{\mathbf{w}_1^T\mathbf{S}\mathbf{w}_1}{\mathbf{w}_1^T\mathbf{N}\mathbf{w}_1} = \frac{1}{\mathbf{w}_1^T\mathbf{N}\mathbf{w}_1}\mathbf{w}_1^T\mathbf{S}\mathbf{w}_1$$

$$= \left(\frac{1}{\sqrt{\mathbf{w}_1^T\mathbf{N}\mathbf{w}_1}}\mathbf{w}_1\right)^T \mathbf{S}\left(\frac{1}{\sqrt{\mathbf{w}_1^T\mathbf{N}\mathbf{w}_1}}\mathbf{w}_1\right)$$

$$\overset{(C.5)}{>} \frac{\mathbf{w}_2^T\mathbf{S}\mathbf{w}_2}{\mathbf{w}_2^T\mathbf{N}\mathbf{w}_2} = \mathbf{w}_2^T\mathbf{S}\mathbf{w}_2.$$

In this case, $\mathbf{w}_2$ could not be the optimal solution to (C.4), since for

$$\mathbf{w}_3 := \left(\frac{1}{\sqrt{\mathbf{w}_1^T\mathbf{N}\mathbf{w}_1}}\mathbf{w}_1\right)$$

it holds that

$$\mathbf{w}_3^T\mathbf{N}\mathbf{w}_3 = 1$$

and

$\mathbf{w}_3^T \mathbf{S} \mathbf{w}_3 > O_2$.

This contradicts our assumptions and a solution to (C.4) is therefore a solution to (C.2) as well.

We continue by defining optimality conditions for the optimization problem (C.4) using its Lagrangian function

$$\mathscr{L}(\mathbf{w}, \lambda) = \mathbf{w}^T \mathbf{S} \mathbf{w} - \lambda(\mathbf{w}^T \mathbf{N} \mathbf{w} - 1)$$

, where for the optimal argument $\mathbf{w}^*$ all partial derivatives must vanish. Hence,

$$\frac{\partial \mathscr{L}}{\partial \mathbf{w}} = 2\mathbf{S}\mathbf{w} - 2\lambda \mathbf{N}\mathbf{w} \stackrel{!}{=} 0$$

$$\frac{\partial \mathscr{L}}{\partial \lambda} = -\mathbf{w}^T \mathbf{N} \mathbf{w} + 1 \stackrel{!}{=} 0.$$

It can be seen that the conditions lead to the generalized eigenvalue problem in (C.3).

Some generalized eigenvalue problems can be converted to standard eigenvalue problems by multiplication with $\mathbf{N}^{-1}$. In this case, the optimal spatial filter $\mathbf{w}^*$ can be found as the eigenvector corresponding to the largest eigenvalue. However, in many cases the conversion to a standard eigenvalue problem is problematic. Although $\mathbf{N}$ is generally invertible, the matrix $\mathbf{N}^{-1}\mathbf{S}$ of the corresponding standard eigenvalue problem is not necessarily symmetric.

According to detailed considerations of this problem (Shawe-Taylor and Cristianini, 2004; Haufe et al., 2014; Banerjee and Roy, 2014), it is preferable to compute the standard eigenvectors $\mathbf{v}_i$ of an alternative matrix $\mathbf{M}$

$$\mathbf{M} := \mathbf{N}^{-\frac{1}{2}} \mathbf{S} \mathbf{N}^{-\frac{1}{2}}$$

and recollect the solutions to the original problem as

$$\mathbf{w}_i = \mathbf{N}^{-\frac{1}{2}} \mathbf{v}_i.$$

If the columns of $\mathbf{W}$ contain the various $\mathbf{w}_i$ sorted in decreasing order according to their eigenvalues, the corresponding spatial topographies are contained in the rows of $\mathbf{A} = \mathbf{W}^{-1}$.

Appendix C.3. Simulation Task

For each input signal a mixing matrix $\mathbf{A} \in \mathbb{R}^{20\times 20}$ with standard normal entries was generated for the noise sources, resulting in 20 noise mixtures in which the target still had to be added. In a second step, the average power of these noise mixtures was determined, such that in a final step the target oscillation was added to each of them with a specific weight: This target weight was chosen as to enforce a particular SNR value with the average power of the previously computed 20 noise mixtures, thereby implementing a particular task difficulty.

Appendix D. EEG Data

All control subjects were taken from the general public and had to meet specific inclusion criteria regarding their medical history. Patients had recently been diagnosed with first-episode schizophrenia, and were recruited through the Psychosis Center of the Department of Psychiatry at UKE. The EEG data was recorded using 64 Ag/AgCl electrodes positioned according to the 10–20 system, with additional electrode positions AF7,AF3, AF4, AF8, F5, F1, F2, F6, F10, FT9, FT7, FC3, FC4, FT8, FT10, C5, C1,C2, C6, TP7, CPz, TP8, P5, P1, P2, P6, PO3, POz and PO4 mounted on an EEG cap (ActiCaps, Brain Products, Munich, Germany), Impedance was kept below 5kΩ throughout the experiments and EEG data was recorded using the Brain Vision Recorder software version 1.10 (Brain Products, Munich, Germany). From all subjects we recorded 10 min of resting-state activity with eyes closed at 1 kHz sampling frequency.

Appendix E. Kernel Density Estimation (KDE)

Appendix E.1. KDE Basics

KDE can be used to estimate the probability density function of a variable while avoiding any a priori assumptions about the type of distribution it follows. The KDE estimate $q(x)$ of the probability density function $p(x)$ of an i.i.d. sample $x^{(1)}, \ldots, x^{(N)} \in \mathbb{R}$ takes the form

$$q(x) = \frac{1}{Nh} \sum_{n=1}^{N} k\left(\frac{x - x^{(n)}}{h}\right),$$

where k denotes a kernel function, which is often taken to be a Gaussian kernel

$$k(x) = \frac{1}{\sqrt{(2\pi)}} \exp\left(-\frac{1}{2}x^2\right), x \in \mathbb{R}.$$

KDE thus centers a Gaussian density on each sample point and uses their average at a location x to compute $q(x)$. The bandwidth parameter h

represents the standard deviations of the individual Gaussian densities and controls the smoothness of the resulting density estimate: Larger bandwidths h cause the influence of individual samples to broaden. For our estimates, we selected the bandwidth determined by Matlab's *ksdensity* function.

Appendix E.2. Estimation of Bicoherence Distribution with KDE

The goal was to compute the probability of observing components with strong bicoherence peaks at particular locations on the axial-sagittal intersection line. For this reason, components with strong bicoherence peaks should have a larger contribution to the probability estimates than components with weak bicoherence peaks. To achieve this, we applied the following multiplication to the data: For a density estimation based on a set of components Z, the feature of a component $y(t)$ was replicated R_y times, where

$$R_y := \left\lfloor 10^2 \cdot \left(\frac{\Phi(H_{11})}{\langle \Phi(H_{11}) \rangle_{z \in Z}} + \frac{\Phi(H_{12})}{\langle \Phi(H_{12}) \rangle_{z \in Z}} + \frac{\Phi(H_{13})}{\langle \Phi(H_{13}) \rangle_{z \in Z}} \right) \right\rfloor .$$

This quantity relates the strength of all three bicoherence peaks to their respective group average in Z. The sum was further multiplied by a factor 10^2 and R_y was set to the closest lower integer of this value. The density estimates based on components of controls, as well as the estimates based on the combined data, showed a clear bimodal structure with a minimum around $\mathrm{LMCD}_y = -3.5$ (Fig. 5B). In contrast, the density estimate based on patient data did not show a clear bimodality.

We used the minimum of the combined bimodal density, to sort components into two categories: Components with LMCD_y-coordinates $>$ -3.5 were classified as central, while the others were classified as non-central.

Appendix F. Artefact Removal

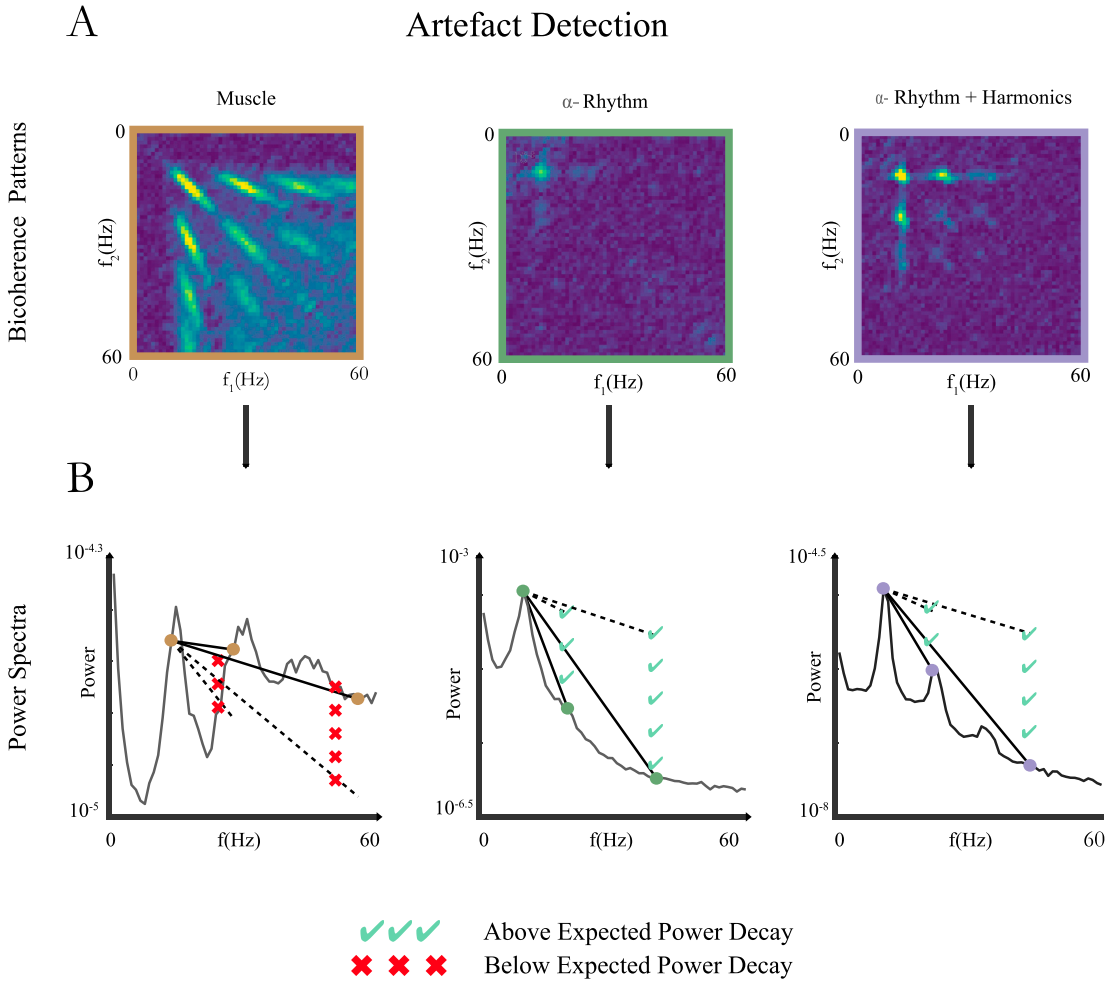

Fig. F.9. (A) Typical bicoherence patterns of alpha rhythms and muscle activity.**(B)** Power spectra associated with bicoherence patterns in (A). Deviations from an expected $1/f$-type power decay are used to recognize signals, which do not originate from brain activity.

Physiological phenomena, like heartbeat and muscle activity, produce distinctive bicoherence signatures at frequencies in the alpha range. We refer to such non-neurophysiological components as artefactual components. In general, HPMax was designed, to extract signal components representing alpha oscillations. Nonetheless, if no such oscillation is present in the original signal, or if the alpha rhythm is weak, the HPMax criterion might be optimized by artefactual components, instead. For this reason, we used two weak criteria to sort out unwanted components:

1. Power spectra of human EEG recordings typically show a decay of power over frequencies, which resembles the power decay of $1/f$-noise. For each component, this power decay should not be weaker, than it is the case for $1/f$-noise. We therefore enforce that $P(f_{2p})/P(f_p) \leq 1/2$ and

$P(f_{4p})/P(f_p) \leq 1/4$. Thus, we check the power at two locations in frequency space and ensure, that the power decay is not smaller than the power decay expected for $1/f$-noise.

2. The $LMCD_y$ coordinate of a component should be < 1, to avoid a predominant influence of eye movements.

We illustrate the second criterion using three signal types, one of which arises from muscle activity, while the other two represent actual alpha rhythms (Fig. 5C and D). The two alpha oscillations differ in the strength of their power-spectral- and bicoherence peaks at higher harmonics. For each signal, the values $P(f_p)$, $P(f_{2p})$ and $P(f_{4p})$ are marked on the respective power spectrum, connected by a solid line, if two power values are compared to each other. The dotted lines between the same frequency values represent the power decay, that would be expected in the case of pure $1/f$-noise over a frequency interval of this length. While both alpha rhythms meet the before mentioned criteria with ease, the muscle spectrum is excluded at this step due to its deviation from a $1/f$-law power decay (Fig. 5D).

Appendix G. Identification of Power-Spectral Peaks

To compare our bispectral results to power effects (Section 3.4) we identified alpha peaks in the power spectra of MR-components for patients and controls using MATLAB's *findpeaks* routine. In the case of multiple power-spectral peaks we ensured that the peak frequencies were harmonically related (by an alpha-band frequency $\pm$ 1 Hz). Further we rechecked the identified peaks for each components while blindfolded w.r.t. group membership (no adjustments were made). We characterized each power-spectral peak by its absolute power and its prominence as defined by the *findpeaks* routine (a good explanation can be found under https://de.mathworks.com/help/signal/ref/findpeaks.html#buff2uu).

References

Avarvand, F.S., Bartz, S., Andreou, C., Samek, W., Leicht, G., Mulert, C., Engel, A.K., Nolte, G., 2018. Localizing bicoherence from eeg and meg. NeuroImage 174, 352–363.

Banerjee, S., Roy, A., 2014. Linear Algebra and Matrix Analysis for Statistics. CRC Press.

Cohen, M.X., 2017a. Comparison of linear spatial filters for identifying oscillatory activity in multichannel data. J. Neurosci. Methods 278, 1–12.

Cohen, M.X., 2017b. Multivariate cross-frequency coupling via generalized eigendecomposition. ELife 6.

Cole, S.R., Peterson, E.J., van der Meij, R., de Hemptinne, C., Starr, P.A., Voytek, B., 2016. Nonsinusoidal Oscillations Underlie Pathological Phase-amplitude Coupling in the Motor Cortex in Parkinson's Disease bioRxiv, 049304.

Cole, S.R., Voytek, B., 2017. Brain oscillations and the importance of waveform shape. Trends Cognit. Sci. 21, 137–149.

Cole, S.R., Voytek, B., 2018. Cycle-by-cycle Analysis of Neural Oscillations bioRxiv , 302000.

Di Pellegrino, G., Fadiga, L., Fogassi, L., Gallese, V., Rizzolatti, G., 1992. Understanding motor events: a neurophysiological study. Exp. Brain Res. 91, 176–180.

Elgar, S., 1987. Relationships involving third moments and bispectra of a harmonic process. IEEE Trans. Acoust. Speech Signal Process. 35, 1725–1726.

Enticott, P.G., Hoy, K.E., Herring, S.E., Johnston, P.J., Daskalakis, Z.J., Fitzgerald, P.B., 2008. Reduced motor facilitation during action observation in schizophrenia: a mirror neuron deficit? Schizophr. Res. 102, 116–121.

Haufe, S., Meinecke, F., Görgen, K., Dähne, S., Haynes, J.D., Blankertz, B., Bießmann, F., 2014. On the interpretation of weight vectors of linear models in multivariate neuroimaging. Neuroimage 87, 96–110.

Iacoboni, M., Dapretto, M., 2006. The mirror neuron system and the consequences of its dysfunction. Nat. Rev. Neurosci. 7, 942–951.

Jones, S.R., 2016. When brain rhythms aren't âĂŸrhythmicâĂŹ: implication for their mechanisms and meaning. Curr. Opin. Neurobiol. 40, 72–80.

Keysers, C., Kohler, E., Umiltà, M.A., Nanetti, L., Fogassi, L., Gallese, V., 2003. Audiovisual mirror neurons and action recognition. Exp. Brain Res. 153, 628–636.

Kohler, E., Keysers, C., Umilta, M.A., Fogassi, L., Gallese, V., Rizzolatti, G., 2002. Hearing sounds, understanding actions: action representation in mirror neurons. Science 297, 846–848.

Kovach, C.K., Oya, H., Kawasaki, H., 2017. The Bispectrum and its Relationship to Phase-amplitude Coupling. arXiv:1705.10435.

Kramer, M.A., Tort, A.B., Kopell, N.J., 2008. Sharp edge artifacts and spurious coupling in eeg frequency comodulation measures. J. Neurosci. Methods 170, 352–357.

McCormick, L.M., Brumm, M.C., Beadle, J.N., Paradiso, S., Yamada, T., Andreasen, N., 2012. Mirror neuron function, psychosis, and empathy in schizophrenia. Psychiatr. Res. Neuroimaging 201, 233–239.

Muthukumaraswamy, S.D., Johnson, B., 2004. Changes in rolandic mu rhythm during observation of a precision grip. Psychophysiology 41, 152–156.

Muthukumaraswamy, S.D., Johnson, B.W., McNair, N.A., 2004. Mu rhythm modulation during observation of an object-directed grasp. Cognit. Brain Res. 19, 195–201.

Nikulin, V.V., Nolte, G., Curio, G., 2011. A novel method for reliable and fast extraction of neuronal eeg/meg oscillations on the basis of spatio-spectral decomposition. NeuroImage 55, 1528–1535.

Pascual-Marqui, R.D., Pascual-Montano, A.D., Lehmann, D., Kochi, K., Esslen, M., Jancke, L., Anderer, P., Saletu, B., Tanaka, H., Hirata, K., et al., 2006. Exact low resolution brain electromagnetic tomography (eloreta). Neuroimage 31.

Shahbazi, F., Ewald, A., Nolte, G., 2014. Univariate normalization of bispectrum using hölder's inequality. J. Neurosci. Methods 233, 177–186.

Shawe-Taylor, J., Cristianini, N., 2004. Kernel Methods for Pattern Analysis. Cambridge university press.

Sponheim, S.R., Clementz, B.A., Iacono, W.G., Beiser, M., 2000. Clinical and biological concomitants of resting state eeg power abnormalities in schizophrenia. Biol. Psychiatry 48, 1088–1097.

Ziehe, A., Müller, K.R., 1998. Tdsep: an efficient algorithm for blind separation using time structure. In: ICANN 98. Springer, pp. 675–680.